Carbon 160 (2020) 236–246

Contents lists available at ScienceDirect

Carbon

journal homepage: www.elsevier.com/locate/carbon

In situ Electron paramagnetic resonance spectroelectrochemical study of graphene-based supercapacitors: Comparison between chemically reduced graphene oxide and nitrogen-doped reduced graphene oxide

Bin Wang [a], Vlassis Likodimos [b], Alistair J. Fielding [c, *], Robert A.W. Dryfe [a, d, **]

[a] Department of Chemistry, University of Manchester, Oxford Road, Manchester, M13 9PL, United Kingdom
[b] Section of Solid State Physics, Department of Physics, National and Kapodistrian University of Athens, Panepistimiopolis, 15 784, Greece
[c] School of Pharmacy and Biomolecular Science, Liverpool John Moores University, James Parsons Building, Byrom Street, Liverpool, L3 3AF, United Kingdom
[d] National Graphene Institute, University of Manchester, Oxford Road, Manchester M13 9PL, United Kingdom

ARTICLE INFO

Article history:
Received 26 July 2019
Received in revised form
2 December 2019
Accepted 18 December 2019
Available online 23 December 2019

ABSTRACT

An *in situ* electrochemical electron paramagnetic resonance (EPR) spectroscopic study of N-doped reduced graphene oxide (N-rGO) is reported with the aim of understanding the properties of this material when employed as an electrical double-layer capacitor. N-rGO shows a capacitance of 100 F g^{-1} in 6 M KOH, which is twice that found for reduced graphene oxide (rGO). The temperature dependence of the rGO EPR signal revealed two different components: a narrow component, following the Curie law, was related to defects; and a broad curve with a stronger Pauli law component was attributed to the spin interaction between mobile electrons and localised π electrons trapped at a more extended aromatic structure. The N-rGO sample presented broader EPR signals, indicative of additional contributions to the resonance width. *In situ* EPR electrochemical spectroscopy was applied to both samples to relate changes in unpaired electron density to the enhanced capacitance. The narrow and broad components increased and diminished reversibly with potential. The potential-dependent narrow feature was related to the generated radical species from corresponding functional groups: e.g. O- and N-centred radicals. Improved capacitance seen for the N-modified basal graphene planes can be accordingly suggested to underlie the enhanced capacitance of N-rGO in basic electrolytes.

1. Introduction

Electrical energy storage systems include the secondary battery and the supercapacitor. Secondary batteries (such as lithium and sodium ion batteries) have a higher energy density, while supercapacitors have garnered much attention because of their higher power density, long cycling ability and good rate capability [1–3]. Carbon based materials, including porous activated carbon, graphene and carbon nanotubes, are potential active materials due to their high specific surface area and high conductivity [1,4–6]. Heteroatom doping and functionalization have been shown to increase the capacitance of carbon nanomaterials. For example, N-doped graphene (NG) has been shown to have a higher gravimetric capacitance, of up to 300 F g^{-1}, as well as a high rate capability [7–10]. This performance enhancement was attributed to increased conductivity (graphitic-N) and pseudo-capacitive behaviour (pyridinic-N and pyrrolic-N functional groups) [7–11]. Density functional theory and classical molecular dynamic studies provide further evidence that N doping increases the quantum capacitance near the Fermi level, however, detailed experimental studies of the pseudo-capacitive process are still scarce [12–15].

Electron paramagnetic resonance (EPR) spectroscopy is a sensitive spectroscopic probe of the interplay of localised and itinerant spins in carbon nanomaterials and their modifications upon integration as active components in devices, including graphene derivatives where defects, such as vacancies and zigzag states, are recognised as the main source of magnetism [16–22]. A recent magnetisation and EPR study of chemically reduced graphene oxide (rGO), showed that the rGO EPR spectrum comprised two independent spectral components [22]. A narrow EPR resonance at

* Corresponding author.
** Corresponding author. Department of Chemistry, University of Manchester, Oxford Road, Manchester, M13 9PL, United Kingdom.
E-mail addresses: a.j.fielding@ljmu.ac.uk (A.J. Fielding), robert.dryfe@manchester.ac.uk (R.A.W. Dryfe).

https://doi.org/10.1016/j.carbon.2019.12.045

g = 2.0027, broader than pristine graphene oxide (GO), with essentially Curie-like spin susceptibility associated with edge/vacancy defect spins, was superimposed on a broad signal at g = 2.0015 with a higher Pauli contribution to the spin susceptibility. The latter EPR signal was related to defect states, such as localised π electrons trapped by defects or vacancies, strongly coupled with itinerant spins within extended aromatic domains, indicative of rGO's persistent structural inhomogeneity [22,23]. Recent work by Augustyniak-Jabłokow et al. has discussed the origin of the EPR lineshape of GO, and forbidden transitions in the hyperfine structure have been proposed as a source of the line broadening in GO and rGO [19,21].

Heteroatom doping has been pursued as a promising route to enhance and modulate the magnetic response of graphene nanomaterials. Specifically, while potassium doping on rGO may promote Pauli paramagnetism by means of electron transfer, similar to conventional graphitic materials [24], nitrogen doping has been reported as a highly efficient modification to boost the magnetisation on both GO and rGO [25,26], although the microscopic origin of the observed enhancement is complicated by the contribution of pyrollic and graphitic N configurations [25–27]. N-doping has been reported to induce ferromagnetism in GO [25] as well as increase spin-spin/spin-lattice relaxation of nanocarbon based materials [28].

The application of *in situ* techniques, such as electrochemical quartz crystal microbalance (EQCM) and nuclear magnetic resonance (NMR), helps to elucidate ion dynamics, which is particularly relevant when such materials are employed as electrodes for supercapacitors and other energy storage systems [29–32]. For example, *in situ* NMR has provided insights into ionic diffusion and the exchange processes in the nanoporous structure [30–32]. *In situ* EPR provides an analogous probe of (unpaired) electron density and dynamics but its application as a probe of the electrical double layer of carbon based materials is relatively rare [33–36]. *In situ* EPR studies of activated carbon in organic electrolyte found that the EPR signal was potential independent [33]. Similar studies on carbon black found localised radicals from oxygen-related functionalities during electrochemical reduction and delocalised electrons on non-oxidised carbon black in methylene chloride electrolyte [34–36]. Pseudo-capacitive behaviour in carbon based materials can increase the total capacitance efficiently, and EPR spectroscopy is a powerful technique to explore this behaviour [37–40]. More importantly, *in situ* EPR can distinguish between pseudo-capacitive processes and ionic adsorption in aqueous electrolytes [38].

Here, *in situ* EPR is used to study the enhanced electrochemical performance imparted by elemental nitrogen doping on graphene. N-rGO and rGO were prepared by a hydrothermal method with different reducing agents, and N-rGO was found to have twice the specific capacitance of rGO. EPR lineshape simulation, together with temperature dependent measurements, helped to separate the nature of spins on N-rGO and rGO. The present study uses an *in situ* EPR cell that has been previously described [38] and helps to further the understanding of the electrochemical behaviour of different graphene materials.

2. Materials & methods

All chemicals were of analytical grade from Sigma-Aldrich and were used without further purification.

2.1. Preparation of N-doped reduced graphene oxide and chemically reduced graphene oxide

Graphene oxide was prepared by the modified Hummer's method and was further washed under alkaline conditions to remove Mn impurities [41]. N-doped reduced graphene oxide (N-rGO) was prepared by the hydrothermal method according to previous reports, with hydrazine used as the N source [42]. Normally, the mixture of hydrazine monohydrate (1 mL) and GO suspension (2 mg mL^{-1}, 30 mL) was sonicated for half an hour. The mixture was then transferred to a Teflon-lined autoclave and heated for 12 h at 180 °C. The obtained sample was washed with water and collected by filtration. Then, the wet sample was freeze dried (−55 °C and 1 mbar vacuum, Alpha 1–2 LDplus freeze drier, Martin Christ Gefriertrocknungsanlagen GmbH, Germany) to give the final N-rGO powder. The rGO was prepared by the same method except hydrazine was replaced by sodium borohydride with the same solid reductant molar ratio. Finally, the prepared N-rGO, or rGO, was dispersed in *iso*-propyl alcohol/water (volume ratio 1:1) with sonication treatment (37 kHz, 350 W effective power, Fisherbrand FB11205 Ultrasonic Cleaner) for 1 h. The membrane of the resultant active material was prepared by filtration on a PTFE film (25 mm hydrophilic PTFE membrane filter with 0.1 μm pore size and thickness of 140 μm, Merck Millipore Company), and the working electrode was prepared as described in our previous report [38].

2.2. Electrochemical measurements

The electrochemical measurements were carried out with a three electrode system, using Ag|AgCl as a reference electrode, in 6 M KOH. The specific capacitance (C_s) can be assessed from a cyclic voltammogram (CV) (Equation (1)) or from the galvanostatic discharge (Equation (2)) response:

$$C_s = \frac{\int IdV}{2m\nu\Delta V} \tag{1}$$

$$C_s = \frac{It}{m\Delta V} \tag{2}$$

where ν is the scan rate, $\frac{1}{2} * \int IdV$ is the integral of half of the CV cycle with respect to potential, ΔV is the cell voltage range, m is the mass loading of the electrode, I is constant current and t is the discharge time.

2.3. In situ EPR experiments

The *in situ* EPR cell was also based on a three electrode system, as previously described: Pt mesh and Ag|AgCl were used as the counter and reference electrodes, respectively [38]. The electrolyte was anaerobically treated, and the cell was assembled under a N_2 atmosphere in a glove box. Supporting materials, such as PTFE membrane and the Pt wire, were found to be EPR silent [38]. The prepared cell was cycled 20 times (using CV at 50 mV s^{-1}, with the same potential window as used for the active samples, in 6 M KOH) to obtain a stable response before the *in situ* EPR experiment. The potential waveforms were applied using a potentiostat ($EmStat^{3+}$ Blue, PalmSens, the Netherlands). The EPR spectra were recorded using a continuous-wave (CW) Bruker micro EMX spectrometer at room temperature. In all cases, the microwave frequency was approximately 9.8 GHz, and the modulation amplitude was 4 G, and the microwave power was typically 2 mW. Triplicate samples were recorded for the *in situ* EPR experiment, each averaged over 20 scans. The Q value of the electrode under various potentials was monitored using a ruby placed inside the cavity and was found to be stable [38]. The EPR signal of N-rGO/rGO decayed over time in 6 M KOH aqueous electrolyte, owing to chemical quenching of the radical species [41]. For example, the signal intensity decreased by

around 10% when the powder sample was immersed in the electrolyte for one week [41]. In order to minimize the intrinsic signal decay during the *in situ* measurement, the assembled cell was left for 24 h before use.

2.4. Ex situ EPR temperature dependence experiments

The *ex situ* temperature-dependent experiments of the powder rGO/N-rGO samples were carried out in a range between 4.2 K and 150 K under non-saturating conditions (Fig. S1). Temperature calibration was carried out using a temperature sensor (Cernox®, Lake Shore Cryotronics, Inc.) inserted into the sample position. Error bars reflect duplicate runs and the estimated temperature uncertainty. Experiments to observe the effect of an applied potential on the temperature dependence were made with the electrode frozen immediately (within 5 s) in liquid nitrogen after applying the potential for 5 min (under non-saturating conditions, Fig. S2). The assumption is that the potential distribution is maintained, to some extent, and therefore the low temperature experiment retains some information about the state of the system under the applied potential. In support of this approach, previous studies on activated carbon indicated that the return to equilibrium after removal of the applied voltage was relatively long (timescale of hours) [38].

2.5. Characterization

The SEM analysis was carried out using an FEI Quanta 650 FEG environmental scanning electron microscope. X-ray photoelectron spectroscopy (XPS) was performed using a Kratos Axis Ultra DLD spectrometer with a monochromated Al Kα X-ray source (E = 1486.6 eV, 10 mA emission).

3. Results

3.1. XPS characterization of rGO and N-rGO

XPS was used to confirm the distribution of elements in both rGO and N-rGO samples. rGO and N-rGO were prepared via the hydrothermal method by using different reductants, as described above. Both materials are seen to possess a three-dimensional (3D) porous structure (Fig. S3) due to the self-assembly of GO nanosheets and the freeze drying process [10,43,44]. XPS was used to confirm the elemental compositions and nitrogen bonding configurations in N-rGO and rGO. As shown in Fig. 1a, the peaks at 284.5 eV and 532.5 eV correspond to C 1s and O 1s, respectively [45–49]. Only N-rGO presents the N 1s peak at 399.5 eV with the atomic N percentage of 4%, indicating successful nitrogen doping of graphene. The C1s peak of N-rGO can be fitted to four components (Fig. 1b), corresponding to the C═C/C–C, C–N, C═O/N–C═O, O–C═O and the π-π* shakeup from sp^2 (aromatic) carbon located at 284.5, 285.8, 287.8, 288.9 and 291.5 eV, respectively. Similarly, the N 1s peak in N-rGO has three components, centred at 398.5 eV, 400.1 eV and 401.5 eV, corresponding to pyridinic-N, pyrrolic-N, and graphitic-N (Fig. 1c), while no nitrogen groups were found in rGO (Fig. 1d).

3.2. EPR characterization of solid state rGO and N-rGO

The origin of the spins in rGO and N-rGO samples were studied by temperature dependent EPR experiments using lineshape simulation, over the range of 4.2 K–170 K (Fig. S4) under non-saturating conditions.

The rGO sample showed a composite resonance lineshape with a turning point at g = 2.0038 close to the free electron (g_e = 2.0023) across the temperature range. The origin of the EPR signal of rGO was corroborated by the temperature dependence of the corresponding spin susceptibilities (χ), determined from the double integral of the first-derivative EPR signal for each resonance. The χ can be fitted with the sum of Curie-Weiss law from localised spins and a temperature independent Pauli contributions (χ_0):

$$\chi = \chi_0 + C/(T-\Theta) \quad (3)$$

Where C is the Curie-Weiss constant and Θ is the Curie-Weiss temperature. The χ of rGO samples can be fitted using Equation (3) with C_{rGO} = 1.2 (1) × 10^{-5} emu K g^{-1}, Θ_{rGO} = −9.3 (8) K and the constant term, $\chi_{0\text{-}rGO}$ = 4.4 (5) × 10^{-8} emu g^{-1}. The spin density of rGO calculated from the Curie-Weiss constant was 1.9 (2) × 10^{19} spins g^{-1}. This is a similar value to that measured by Diamantopoulou et al. [22] The composite nature of the EPR signal was revealed as a function of temperature. For example, the EPR signal of rGO (e.g. 20 K, Fig. 2b) could be fitted well to the sum of two independent Lorentzian or Dysonian components (Fig. S5): a broad (B) resonance superimposed on a narrow (N) one, which largely determined the central EPR peak. The narrow EPR resonance had a g value of 2.0038 (2) and was temperature independent (Fig. S6a). The peak-to-peak linewidth initially decreased from 170 K to 30 K (from 6.5 G to 5.4 G) and then increased on further lowering of the temperature (5.9 G at 5 K, Fig. S6a). Previous work has found that reduced graphene oxide had a relatively small EPR linewidth, which remained approximately constant down to 50 K indicative of isolated spins. This was thought to be due to a narrowing mechanism that effectively reduced dipolar broadening and other inhomogeneous contributions to the resonance width [22]. In our case the narrowing of line width may arise through changes in the exchange, thereby causing a change in the motional narrowing phenomenon [22]. The broad signal came into resonance at g = 2.0040 (20) (Fig. S5) and had considerably greater linewidth that decreased almost linearly with the decreasing temperature (Figure S6b, 120 G at 170 K and 22 G at 5 K) indicating the dominance of relaxation processes [23,50–52].

The nature of the two different signals was further analysed by the spin susceptibilities $\chi(T)$ as shown in Fig. 2c and d. The narrow component (Fig. 2c) closely followed Curie-Weiss behaviour with C^N_{rGO} = 5.1 (8) × 10^{-7} emu K g^{-1}, Θ^N_{rGO} = −7.1 (7) K and $\chi^N_{0\text{-}rGO}$ = 3.2 (2) × 10^{-8} emu g^{-1}, as shown in Table 1. The paramagnetic nature of the narrow component was directly reflected in the temperature variation of the product $\chi \times T$ (inset in Fig. 2c) which increased weakly down to 50 K, below which a maximum was observed at ca. 20 K. This behaviour is characteristic of localised spins with weak antiferromagnetic interactions (signalled by the negative Curie-Weiss temperature) and possibly the contribution of a high spin state producing the maximum as has previously been reported [22]. The broad curve (Fig. 2d) showed similar Curie-Weiss $\chi(T)$ variation together with a Pauli contribution with C^B_{rGO} = 5.4 (8) × 10^{-7} emu K g^{-1}, Θ^B_{rGO} = −8.7 (1) K and $\chi^B_{0\text{-}rGO}$ = 1.3 (3) × 10^{-8} emu g^{-1}, which supports the interpretation of the influence of itinerant electrons in sp^2 domains.

Qualitatively similar results were obtained for the N-rGO powder (Fig. S7, Fig. 3b and Table 1), whose EPR signal at g = 2.0033 (4) could be simulated by two independent Lorentzian components, a broad and narrow resonance. Greater linewidths were found for the N-rGO powder compared to those of rGO (Figs. S8–S9, Table 1). The normalised signal intensity for N-rGO was found to be less than that of rGO by around 60%. Further results from out-of-phase experiments following the work of Augustyniak-Jabłokow et al. did not show any evidence for forbidden transitions and significantly slow relaxation of spins in both N-rGO and rGO materials (Fig. S10) [19,21]. The total spin susceptibility (inset in Fig. 3a) could be also

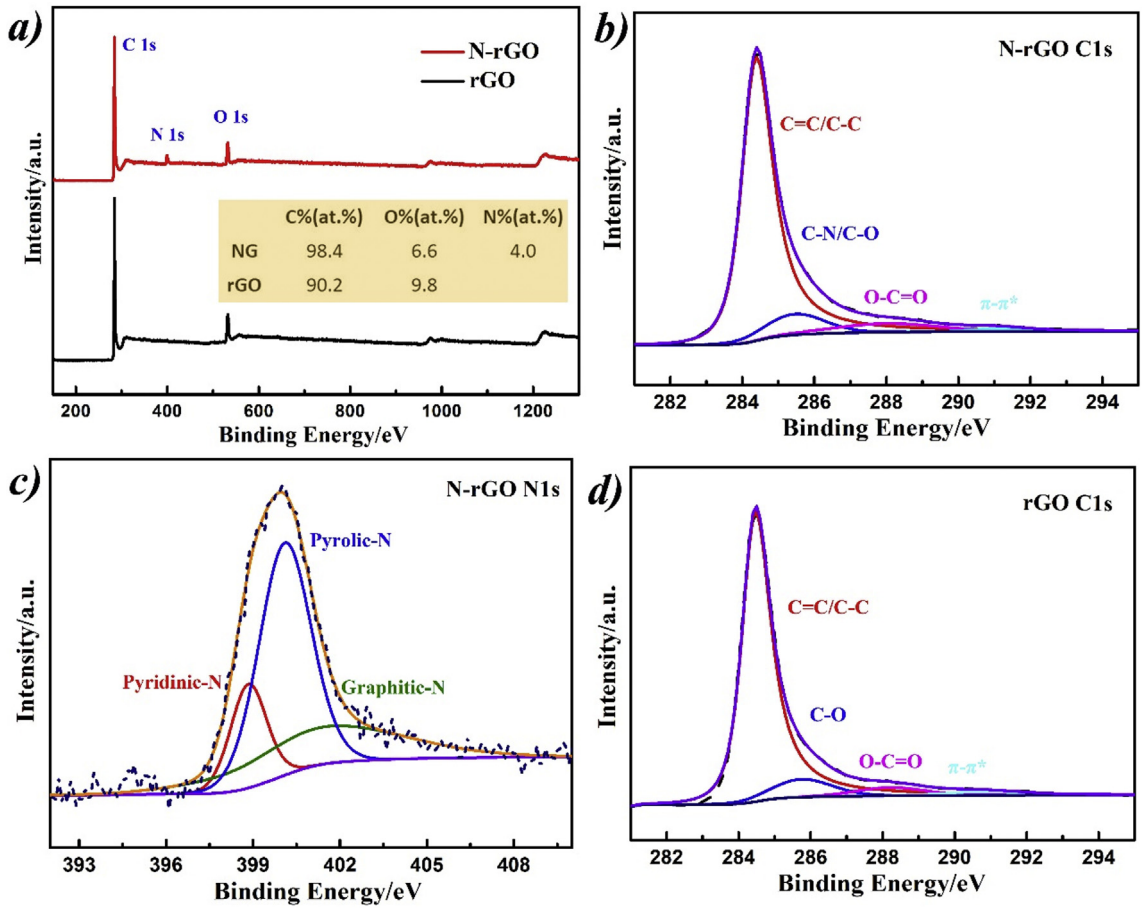

Fig. 1. XPS data for N-rGO and rGO. (a) XPS survey scan spectra of N-rGO and rGO, the inset table shows the elemental content of each sample; (b) C1s and (c) N 1s spectra of N-rGO; (d) C 1s spectra of rGO. (A colour version of this figure can be viewed online.)

fitted to Curie-Weiss behaviour with $C_{N\text{-}rGO} = 6.8\ (6) \times 10^{-6}$ emu K g^{-1}, $\Theta_{N\text{-}rGO} = -0.2\ (1)$ K and $\chi_{0\text{-}N\text{-}rGO} = 3.2\ (5) \times 10^{-8}$ emu g^{-1}, and spin density of 1.1 (2) $\times 10^{19}$ spin g^{-1}. The spin susceptibility of the narrow EPR line (Fig. 3c) with $C^{N}_{N\text{-}rGO} = 2.8\ (1) \times 10^{-6}$ emu K g^{-1}, $\Theta_{N\text{-}rGO}{}^{N} = 1.0\ (4)$ K and $\chi^{N}_{0\text{-}N\text{-}rGO} = 1.8\ (9) \times 10^{-8}$ emu g^{-1}, increased continuously at lower temperature, more quickly than the *1/T* dependence predicted by the simple Curie behaviour (inset of Fig. 3c). This has been previously observed for GO by Ćirić et al. [53] and discussed in terms of increasing interaction between localised moments on decreasing temperature or from thermal excitation of weakly localised spins into the conduction band. The broad EPR component had a strongly temperature dependent linewidth (Fig. S5b) that followed the Curie-Weiss law with $C^{B}_{N\text{-}rGO} = 3.5\ (2) \times 10^{-6}$ emu K g^{-1}, $\Theta^{B}_{N\text{-}rGO} = -0.1\ (3)$ K and considerably higher Pauli contribution compared to the narrow $\chi^{B}_{0\text{-}N\text{-}rGO} = 5.4\ (4) \times 10^{-8}$ emu g^{-1} (Table 1), indicating, again, that the underlying spins most likely arise from electrons trapped by defects at the extended sp^2 aromatic regions of N-rGO [22,38]. Interestingly, the Pauli contribution is less than that for rGO.

3.3. Electrochemical properties of N-rGO and rGO

The electrochemical performance of the prepared N-rGO and rGO was tested using a three-electrode system, in 6 M KOH electrolyte, with the N-rGO and rGO used as the working electrodes to study the effect of N-doping.

The CV of the rGO and N-rGO electrodes was analysed as a function of scan rate (see Fig. S11), which led to a gravimetric capacitance of 100 F g^{-1} being calculated for N-rGO, whereas rGO presented a gravimetric capacitance of 45 F g^{-1} at 10 mV s^{-1} (Fig. 4a), which is consistent with previous reports [7,45,46]. According to the charge/discharge curves (Fig. 4b), the discharging time of the NG is significantly longer than that of rGO, indicating that N-rGO offers a much larger capacitance, which is again consistent with the conclusions drawn from cyclic voltammetry. The rate performance of N-rGO is shown in Fig. 4c: the calculated capacitance falls from 125 F g^{-1} at 0.2 A g^{-1} to 51 F g^{-1} at 8 A g^{-1}. A comparison of the data with that obtained in previous literature is shown in Table S1. The decrease of specific capacitance with discharge current might be related to ion transport limitations as well as the relatively low conductivity of the electrode [54]. Similarly, the increased capacitance of N-rGO might be related to the improved conductivity from the presence of graphitic N in graphene and the external pseudo-capacitive behaviour from the presence of the pyrrolic N [8,45,46,55,56].

3.4. In situ EPR spectroelectrochemical response of rGO in 6 M KOH

In situ EPR was used to study the Faradaic reactions occurring at the rGO electrode during the electrochemical process, and the ex-situ temperature dependent experiment was adapted to confirm the origin of generated spins.

The EPR spectrum of a rGO electrode in 6 M KOH electrolyte presented a distinct reversible dependence on potential, i.e. a marked increase of the signal intensity during charging that reversibly decreased with the decrease of the applied potential

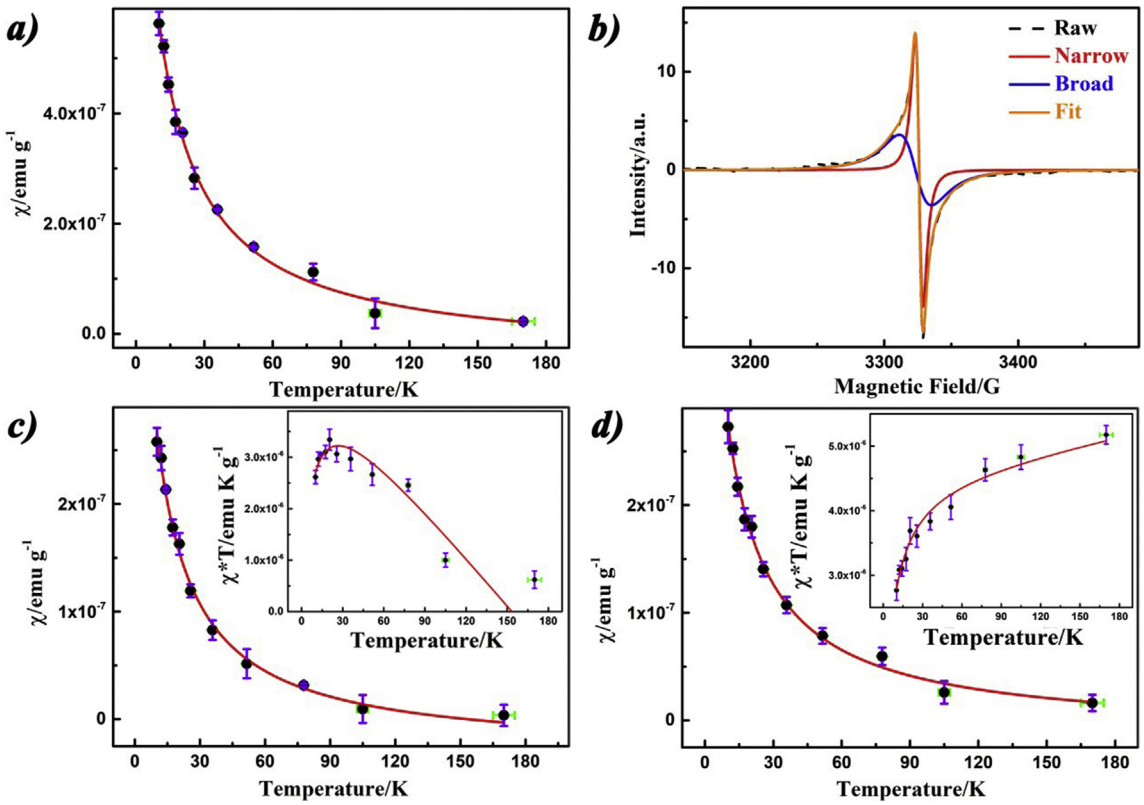

Fig. 2. Temperature dependent results of powder rGO sample. (a) Temperature variation of χ vs T (black dots) of rGO powder; (b) EPR lineshape simulation with two independent Lorentzian curves at 20 K; temperature dependent of the corresponding narrow (c) and the broad (d) component. The red line in (a), (c) and (d) shows the fitting result of the sum of Curie-Weiss and Pauli law. The insets in (c) and (d) show the corresponding temperature variation of $\chi \times T$ vs T results. (A colour version of this figure can be viewed online.)

Table 1
Summary of the XPS derived elemental composition and EPR spin susceptibility of N-rGO and rGO.

		rGO		N-rGO	
Element (%)	**C**	90.2		89.4	
	N	–		4	
	O	9.8		6.6	
Spin Density		1.9 (2) * 10^{19} spins g^{-1}		1.1 (2) * 10^{19} spins g^{-1}	
C (10^{-5} emu K g^{-1})		1.2 (1)		0.68	
Θ (K)		−9.3 (8)		−0.2 (1)	
χ_0 (10^{-8} emu g^{-1})		4.4 (5)		3.2 (5)	
Resonance Components		**Narrow**	**Broad**	**Narrow**	**Broad**
C (10^{-6} emu K g^{-1})		5.1 (8)	5.4 (8)	2.8 (1)	3.5 (2)
Θ (K)		−7.1 (7)	−8.7 (1)	1.0 (4)	−0.1 (3)
χ_0 (10^{-8} emu g^{-1})		3.2 (2)	1.3 (3)	1.8 (9)	5.4 (4)
Width (G) (20 K)		5.6	24.1	8.7	42.8

when discharged (Fig. 5a and b). Line-shape deconvolution indicated the presence of two different components (marked with different colours in Fig. S12), qualitatively similar to the powder rGO EPR. The narrow curve at g ≈ 2.0035 (5) presented a linewidth close to 8 G at −0.8 V with an asymmetric Lorentzian lineshape, with an increase of linewidth up to 20 G at 0 V. The corresponding spin density (calculated by the double integration of the first-derivative signal) of the narrow component (blue lines in Fig. 5c) remained approximately constant at lower potentials, whereas a sudden increase occurred at around −0.4 V. A reversible change of the narrow component was observed during discharging, i.e. the spin density was approximately constant from 0 to −0.3 V, then dropped rapidly from −0.4 to −0.5 V, and finally decreased slightly at −0.8 V. The broad EPR component at g ≈ 2.0020 (8) (Fig. S13) in Fig. 5a and b, presented an asymmetric Lorentzian lineshape with a linewidth of 60 G at −0.8 V that decreased drastically with increasing potential to 20 G at 0 V (Fig. 5 e,f). The changes in the broad EPR component were also reversible with respect to potential, as shown in Fig. 5b. The spin density of the broad spectral feature varied reversibly during the charging/discharging process presenting a weak potential dependence consisting of a small increase/decrease at the low potential range during charging/discharging, as shown in Fig. 5c and d.

In order to explore the physical origin of the unpaired spins, the temperature dependence of the electrochemical EPR spectra for the rGO electrode was measured under applied potentials of −0.7 V and 0 V as shown in Fig. S11. The total spin density of rGO at the different potentials followed the Curie-Weiss behaviour described above. EPR lineshape simulation identified two components at the lower potential of −0.7 V (Figure S14a/b), similar to the powder rGO

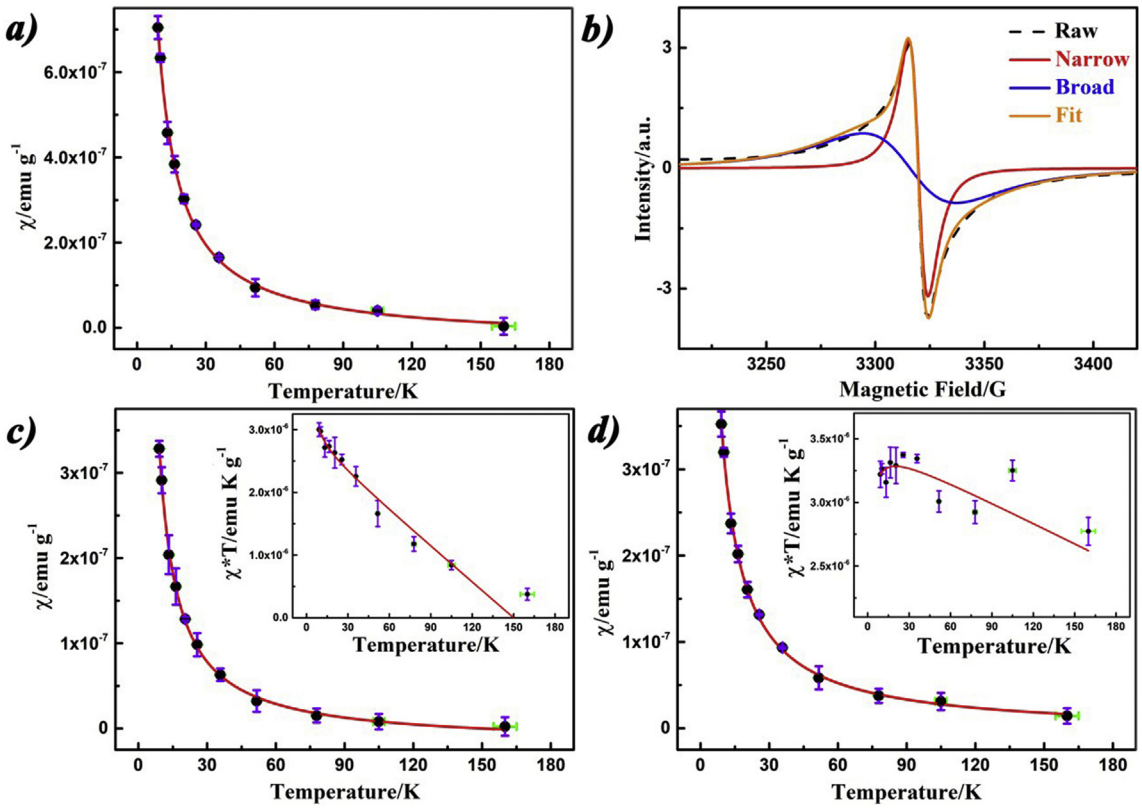

Fig. 3. Temperature dependent results of powder N-rGO sample. (a) Temperature variation of χ vs T (black dots) of rGO powder; (b) EPR lineshape simulation with two independent Lorentzian curves at 20 K; temperature dependence of the corresponding narrow (c) and the broad (d) component. The red line in (a), (c) and (d) shows the fitting result of the sum of Curie-Weiss and Pauli law. The insets in (c) and (d) show the corresponding temperature variation of $\chi \times T$ vs T results. (A colour version of this figure can be viewed online.)

EPR spectra. The narrow component at 0 V showed Curie-Weiss behaviour but with a higher spin susceptibility value (Table S2 and Fig. S14) compared to −0.7 V. The broad EPR component presented standard Curie-Weiss behaviour with a Curie-Weiss temperature of −1.78 K (Table S2). Considerably higher spin density was found at the higher potential of 0 V compared to −0.7 V, as shown in Figure S14c, and a broad EPR component could not be discriminated at temperatures lower than 115 K.

3.5. *In situ EPR spectroelectrochemical response of N-rGO in 6 M KOH*

Again, *in situ* EPR at room temperature and ex-situ temperature dependence experiment was adapted to confirm the origin of generated spins on N-rGO electrode during electrochemical process. The EPR signal of N-rGO changed over potential as shown in Fig. 6 (with the lineshape simulation at various potentials shown in Fig. S15). The EPR signal of N-rGO also showed a reversible potential dependent behaviour during charging (a) and discharging (b). The narrow resonance showed a potential dependence consisting of an increase of intensity at higher potentials (e.g. −0.4 V) during the charging process (and the corresponding decrease during discharge), as shown in Fig. 6c. The linewidth of the narrow EPR line remained constant at about 6.5 G, independent of the applied potential (Fig. S16). The broad EPR component with linewidth over 50 G presented a significant potential dependence (Fig. S16). In particular, the corresponding spin density increased/decreased markedly during the charging/discharging process as shown in Fig. 6c, reaching a two-fold enhancement/reduction as the potential varied. The spin density variation was accompanied by little linewidth change during charging and broadening during discharging (from 50 G at 0 V to 70 G at −0.8 V) indicative of concomitant potential dependent variations of spin dynamics in the N-rGO electrode. Interestingly the lineshapes with applied potential showed more asymmetry compared to the solid samples without applied potential. Mobile electrons within conducting materials (e.g. graphite, graphene) can show a Dysonian lineshape due to the skin effect: the asymmetry parameter can be quantified by the A/B ratio (Fig. S17) [37]. For example, the asymmetric factors of rGO and N-rGO are 1.5 (±0.2) and 2.1 (±0.4), respectively, compared to 1.1–1.2 in the solid state with no applied potential. The asymmetry did not change over the potential range employed.

Temperature-dependent EPR measurements of N-rGO at different potentials were subsequently carried out to investigate the nature of different spins. The magnetic properties of the narrow resonance of N-rGO electrode at −0.7 V/0 V (Fig. S18) were very similar compared to the results of solid N-rGO without applied potential (Fig. 3). This indicates that the nature of two resonances were essentially identical during the electrochemical process. The spin density of the narrow EPR signal increased moderately at 0 V, compared to −0.7 V, reflecting the formation of O/N centred radicals owing to the enhanced oxidation at the higher potential. The broad EPR component at 0 V (Fig. S18, Table S2) exhibited a mixed Curie-Pauli behaviour with the Pauli contribution considerably enhanced compared to −0.7 V, suggesting an increase in the density of delocalised electrons for the N-rGO electrode with increased potential.

4. Discussion

Table 1 summarises the composition and spin susceptibility of the N-doped reduced graphene oxide and reduced graphene oxide

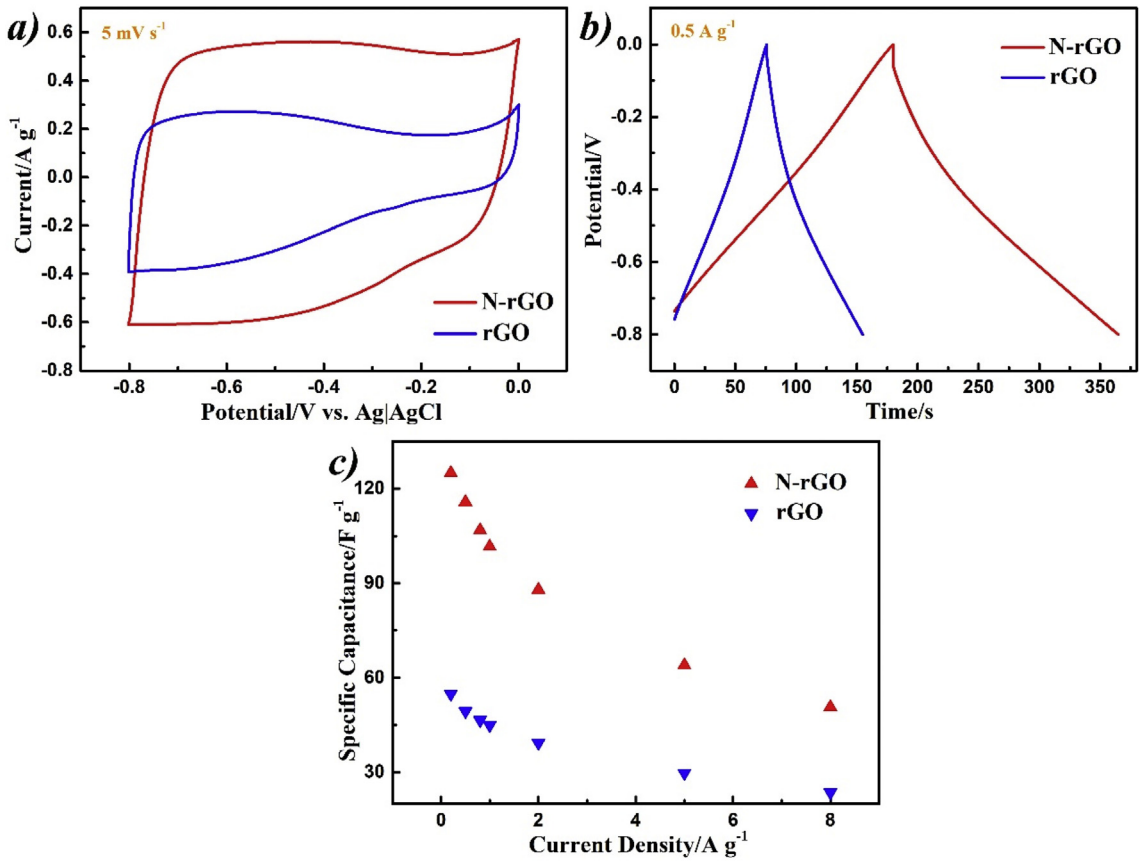

Fig. 4. Compared electrochemical performance of N-rGO and rGO in 6 M KOH. (a) CVs of N-rGO and rGO at a scan rate of 5 mV s^{-1}; (b) galvanostatic charge/discharge curves of N-rGO and rGO at a current density of 0.5 A g^{-1}; (c) specific capacitance calculated from the discharge curve for different electrodes at different scan rates. (A colour version of this figure can be viewed online.)

prepared by the hydrothermal method with different reducing agents. The C 1s XPS results confirmed the presence of N (4%) along with residual O (6%) in N-rGO, while only O (9%) was found in rGO. The nitrogen is distributed on both edges and also defective domains at the basal plane [7,57]. Both samples presented a porous structure on the micrometre scale, formed by the overlap or coalescence of reduced GO nanosheets via π-π stacking interactions. Comparative EPR measurements showed that hydrothermally prepared rGO and N-rGO exhibit a composite resonance lineshape. The g value of rGO (2.0038) is slightly higher than N-rGO (2.0033), matching the higher oxygen content in the rGO samples. The normalised narrow signal of N-rGO was weaker than the corresponding rGO signal, possibly because of reduction in the number of defects. Spectral deconvolution of the EPR lineshape revealed the superposition of two resonances and thus the presence of two distinct spin species for both samples: a narrow signal at a g value close to that of free electron with linewidth around 8 G, and a broad resonance at a slightly higher g value with linewidth above 50 G. The narrow component was attributed to localised spins related to defects and the edge states. The broad component was attributed to π electrons trapped by defects at more extended sp^2 aromatic regions coupled with mobile electrons. Differentiation of the individual EPR signals of localised and itinerant spins is rather difficult at conventional X band (9 GHz) frequencies due to the fast exchange of localised π electrons and delocalised ones that leads to an averaged resonance line [58]. The presence of conduction electrons in both rGO and N-rGO samples was further evident by the temperature variation of the corresponding spin susceptibilities that followed closely the Curie-Weiss law in combination with a Pauli contribution for the broad component (Figs. 2 and 3). Despite the similarities in the EPR spectra for both samples, a small amount of N doping changed the magnetic properties appreciably. The magnetic contribution of nitrogen is effective and complicated [25–27,59,60]. For example, it has been found that pyrrolic-N can introduce external magnetic moments of 0.95 μ_B due to the contribution of π bonds [27,59]. Furthermore, graphitic-N without any magnetic moment can act as a stable attractor, which forms magnetic defects [60], while pyridinic-N contributes less to the magnetic properties [25,26]. Both EPR components in N-rGO were broader than compared to rGO, implying either faster spin relaxation or changes in hyperfine splitting and strain imparted by the presence of pyrrolic and graphitic N-doping. Moreover, the narrow EPR component of N-rGO exhibited less antiferromagnetic properties evident from the less negative Curie-Weiss temperature [54,61,62].

Comparative electrochemical measurements showed that N-rGO possesses a higher specific capacitance (100 F g at 10 mV s^{-1}), twice that of the rGO sample. The electrochemical performance of N-rGO is lower than some earlier reports, especially compared to literature reports for acidic electrolytes (e.g. H_2SO_4). This is related to the limited pseudo-capacitance from functional groups (e.g. quinone, pyrrolic) in proton-free electrolyte (e.g. 6 M KOH) [63,64]. The *in situ* EPR study found a reversible change of the narrow spectral component (Figs. S12 and S15) in both rGO and N-rGO samples. The enhancement of the narrow component can be accordingly attributed to the formation of carbon-oxygen centred radical species on the oxidation of hydroquinone groups/or carboxylate functionalities and also N-centred radical species, for

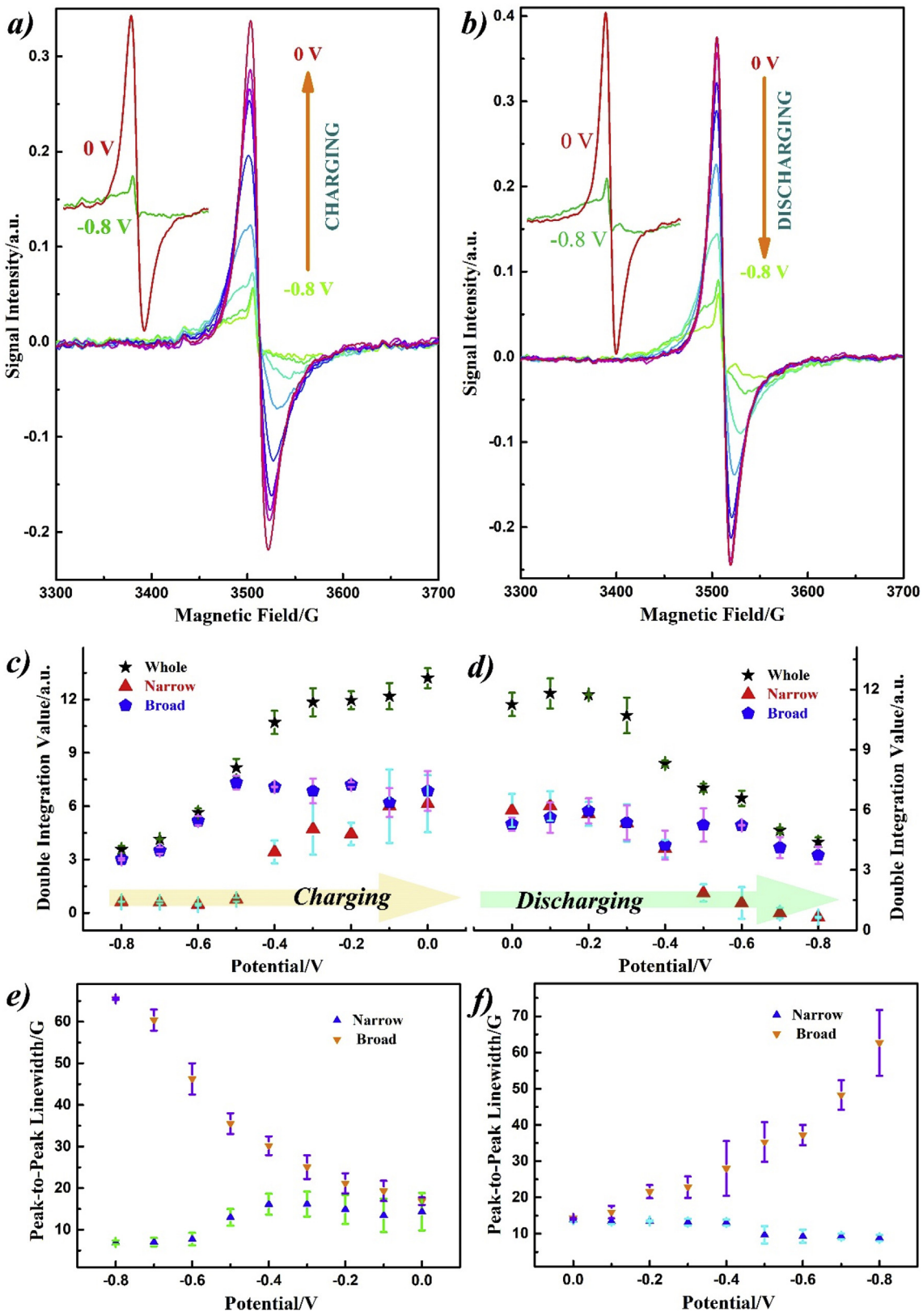

Fig. 5. *In situ* EPR spectral change of rGO from −0.8 to 0 V in 6 M KOH. EPR signal change under various potentials during (a) charging and (b) discharging; the double integral of each component during (c) charging and (d) discharging; the linewidth change during (e) charging and (f) discharging. Inner spectra in (a) and (b) show the comparison of the rGO electrode under 0 V and −0.8 V during charging and discharging. Simulations can be found in Fig. S12. (A colour version of this figure can be viewed online.)

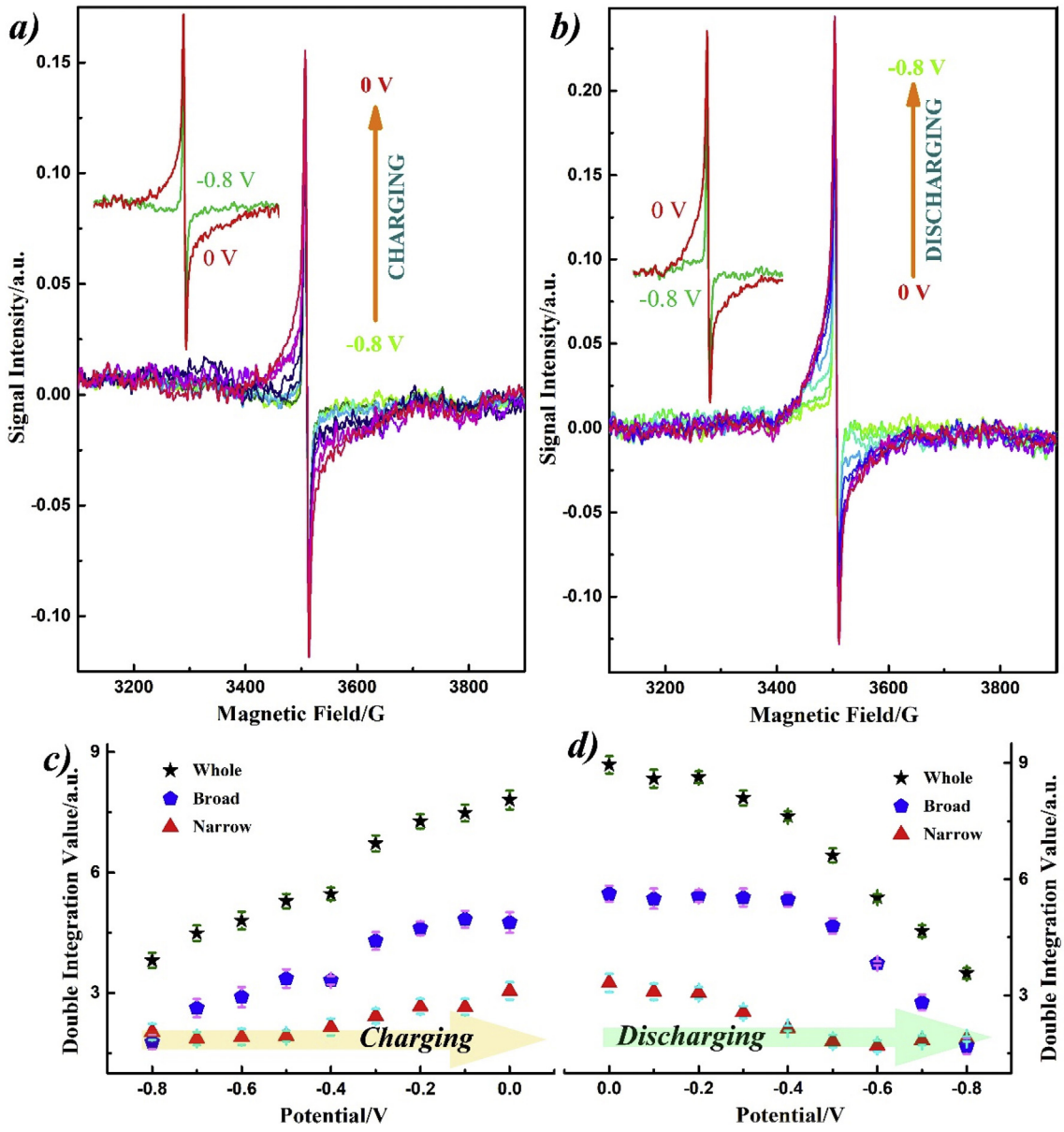

Fig. 6. *In situ* EPR spectra change of N-rGO over potential in 6 M KOH. EPR signal change under various potentials during charging (a) and discharging (b); the double integration value of each component during (c) charging and (d) discharging. Inner curves in (a) and (b) show the comparison of the NG electrode under 0 V and −0.8 V during charging and discharging. (A colour version of this figure can be viewed online.)

example due to the oxidation/reduction of pyrrole-type functionalities under alkaline conditions. However, no significant variation for the g value of the narrow line was observed with the increased potential (Figs. 5 and 6). This might be related to the presence of an averaging of the g value and the relatively low concentration of O centred radicals due to lower O content compared with the reduced sample (confirmed by XPS in Fig. 1) [41]. The relatively localised nature of the narrow signal is confirmed by the temperature dependent results (with the Curie-Weiss fitting in Figs. S13 and S17) and gives further support to the existence of oxygen/nitrogen centred radical species. As N-rGO has a lower O content, the corresponding potential dependence of the narrow EPR component was rather weak. Overall, greater differences were found between the broad resonances for the two materials. The broad component linewidth of the rGO fell significantly with increased potential (Figs. 5 and S13) and this may be explained by differences in the contribution to the linewidth by both the Pauli and the Curie components [65].

Previous reports have studied the potential dependent change in charge carrier density in single layer graphene, where the EPR signal was related to the change in Fermi level around the Dirac point [66]. In this work, temperature dependent results for the broad EPR component as a function of potential suggest that the nature of the underlying spins originates mainly from π electrons localised at more extended aromatic domains. Basal plane defects can be recognised as more extended sp^2 structures (different from the ideal graphene layers and the edge structure) that stabilise π electrons, showing a broad EPR signal. The broad EPR signal is significantly enhanced at higher potentials (Figs. 5 and 6), especially for N-rGO, with the corresponding spin susceptibility at −0.3 to 0 V presenting a marked increase (Table S2) of the Pauli contribution compared with at −0.7 V (Fig. S18a), indicating an enhanced

contribution of itinerant spins. Our previous study of the potential dependent broad signal on activated carbon in 3 M KOH was associated with the ion adsorption into the pore structure [38]. The capacitive process of rGO/N-rGO materials comprises both the pseudocapacitive (the redox peaks shown in CV) and the double layer behaviour (reflecting charge/ion sorption) on the surface. The increased spin density of π electrons localised at more extended sp^2 structures follows a similar trend to the narrow component and may be related to the functional groups on the defective basal plane.

Although the induced pseudocapacitive process can enhance the electrochemical properties of N-rGO, this is not enough to explain the large capacitance enhancement compared with pristine graphene [7,67,68]. Therefore, modifications of the electronic properties arising from N doping should be an important factor. For example, the improved solvent accessibility due to graphitic N in the basal plane (which can disrupt π electrons conjugation) is beneficial for double layer capacitance [67,69]. Double layer capacitance at edge sites is known to be significantly higher than the basal plane contribution, and extra edge sites from N-doping can also contribute to the capacitance [70]. The broad EPR component comprises a major contribution of delocalised spins with a higher spin susceptibility ratio in N-rGO, which presented a higher sensitivity to potential than rGO. We may accordingly conclude that the enhanced electrochemical performance of N-rGO in basic electrolytes is related to the improved electrochemical properties of defective structures (due to the N functionalization at the basal plane) that can be sensitively monitored by *in situ* EPR electrochemical spectroscopy.

5. Conclusions

In this work, *in situ* electrochemical EPR spectroscopy was exploited to probe spin dynamics in N-rGO and rGO supercapacitors, and thereby provide insight to the charging mechanism of N-doped graphene in KOH aqueous electrolytes. Comparative XPS and electrochemical measurements on the hydrothermally prepared N-rGO and rGO confirmed successful N bonding on the graphene layers by pyridinic-N, pyrrolic-N, and graphitic-N functionalities in the former materials, resulting in the doubling of the specific capacitance to a value that exceeded 100 F g^{-1} for the N-rGO electrodes. EPR measurements identified a composite EPR spectrum for both samples, consisting of two distinct resonance lines: a narrow component arising mainly from localised spins at defects and edge states, and a broad component with strongly temperature dependent linewidth, indicative of conduction electron spins coupled with localised π electrons in more extended sp^2 domains. *In situ* electrochemical EPR experiments revealed a reversible variation of the signal intensity during charging/discharging, with the signal intensity increasing with potential for both N-rGO and rGO electrodes, though with distinct differences in the spectral weights of the two components. Considering that the narrow EPR signal arises largely from localised defect spins, corroborated by temperature dependent EPR measurements after the application of different potentials, the increase of the corresponding spin density at high potential was related to the formation of stable radical species such as carbon-oxygen centred radicals in the KOH electrolyte, an effect most pronounced for the rGO electrode with the higher O content. On the other hand, the potential dependent broad signal can be related to the changes in unpaired spin density at more extended aromatic structures (basal plane with defects such as pyridine groups, vacancies). The broad EPR component showed a greater variation over the potential range studied in N-rGO than rGO, which indicates the improved capacitive behaviour resulting from N modification at basal planes.

Author contribution section

Bin Wang: Data curation, Investigation, Writing- Original draft preparation. Vlassis Likodimos: Software, Validation. Alistair J. Fielding: Visualization, Conceptualization, Methodology, Writing. Robert A.W. Dryfe: Visualization, Conceptualization, Methodology, Writing.

Declaration of competing interest

The authors declare that they have no known competing financial interests or personal relationships that could have appeared to influence the work reported in this paper.

Acknowledgement

We thank the National EPSRC EPR service and Facility for support (NS/A000055/1), the EPSRC (UK) for further funding (EP/K016954/1, EP/R023034/1) and the ISCF Faraday Challenge Fast Start project on “Degradation of Battery Materials” made available through grant EP/S003053/1. B.W. is grateful for the award of a President’s Doctoral Scholarship from the University of Manchester. We also acknowledge great technical assistance from Mr. Adam Brookfield.

Appendix A. Supplementary data

Supplementary data to this article can be found online at https://doi.org/10.1016/j.carbon.2019.12.045.

References

[1] G. Wang, L. Zhang, J. Zhang, A review of electrode materials for electrochemical supercapacitors, Chem. Soc. Rev. 41 (2) (2012) 797–828.
[2] B.E. Conway, Electrochemical Supercapacitors: Scientific Fundamentals and Technological Applications, Springer US, New York, 1999.
[3] M. Salanne, B. Rotenberg, K. Naoi, K. Kaneko, P.L. Taberna, C.P. Grey, B. Dunn, P. Simon, Efficient storage mechanisms for building better supercapacitors, Nat. Energy 1 (2016) 16070.
[4] A. González, E. Goikolea, J.A. Barrena, R. Mysyk, Review on supercapacitors: technologies and materials, Renew. Sustain. Energy Rev. 58 (2016) 1189–1206.
[5] Q. Wang, J. Yan, Z. Fan, Carbon materials for high volumetric performance supercapacitors: design, progress, challenges and opportunities, Energy Environ. Sci. 9 (3) (2016) 729–762.
[6] P. Simon, Y. Gogotsi, Materials for electrochemical capacitors, Nat. Mater. 7 (2008) 845.
[7] H.M. Jeong, J.W. Lee, W.H. Shin, Y.J. Choi, H.J. Shin, J.K. Kang, J.W. Choi, Nitrogen-doped graphene for high-performance ultracapacitors and the importance of nitrogen-doped sites at basal planes, Nano Lett. 11 (6) (2011) 2472–2477.
[8] L. Sun, L. Wang, C. Tian, T. Tan, Y. Xie, K. Shi, M. Li, H. Fu, Nitrogen-doped graphene with high nitrogen level via a one-step hydrothermal reaction of graphene oxide with urea for superior capacitive energy storage, RSC Adv. 2 (10) (2012) 4498–4506.
[9] S. Dai, Z. Liu, B. Zhao, J. Zeng, H. Hu, Q. Zhang, D. Chen, C. Qu, D. Dang, M. Liu, A high-performance supercapacitor electrode based on N-doped porous graphene, J. Power Sources 387 (2018) 43–48.
[10] L. Zhang, G. Shi, Preparation of highly conductive graphene hydrogels for fabricating supercapacitors with high rate capability, J. Phys. Chem. C 115 (34) (2011) 17206–17212.
[11] D.W. Wang, F. Li, L.C. Yin, X. Lu, Z.G. Chen, I.R. Gentle, G.Q. Lu, H.M. Cheng, Nitrogen-doped carbon monolith for alkaline supercapacitors and understanding nitrogen-induced redox transitions, Chem. Eur J. 18 (17) (2012) 5345–5351.
[12] E. Paek, A.J. Pak, K.E. Kweon, G.S. Hwang, On the origin of the enhanced supercapacitor performance of nitrogen-doped graphene, J. Phys. Chem. C 117 (11) (2013) 5610–5616.
[13] M. Mousavi-Khoshdel, E. Targholi, M.J. Momeni, First-principles calculation of quantum capacitance of codoped graphenes as supercapacitor electrodes, J. Phys. Chem. C 119 (47) (2015) 26290–26295.
[14] C. Zhan, Y. Zhang, P.T. Cummings, D.E. Jiang, Enhancing graphene capacitance by nitrogen: effects of doping configuration and concentration, Phys. Chem. Chem. Phys. 18 (6) (2016) 4668–4674.
[15] L.L. Zhang, X. Zhao, H. Ji, M.D. Stoller, L. Lai, S. Murali, S. McDonnell,

B. Cleveger, R.M. Wallace, R.S. Ruoff, Nitrogen doping of graphene and its effect on quantum capacitance, and a new insight on the enhanced capacitance of N-doped carbon, Energy Environ. Sci. 5 (11) (2012) 9618–9625.
[16] M. Fujita, K. Wakabayashi, K. Nakada, K. Kusakabe, Peculiar localized state at zigzag graphite edge, J. Phys. Soc. Jpn. 65 (7) (1996) 1920–1923.
[17] T. Enoki, K. Takai, The edge state of nanographene and the magnetism of the edge-state spins, Solid State Commun. 149 (27) (2009) 1144–1150.
[18] K. Takai, T. Suzuki, T. Enoki, H. Nishihara, T. Kyotani, Structure and magnetic properties of curved graphene networks and the effects of bromine and potassium adsorption, Phys. Rev. B 81 (20) (2010) 205420.
[19] M.A. Augustyniak-Jabłokow, K. Tadyszak, R. Strzelczyk, R. Fedaruk, R. Carmieli, Slow spin relaxation of paramagnetic centers in graphene oxide, Carbon 152 (2019) 98–105.
[20] L. Ćirić, A. Sienkiewicz, B. Náfrádi, M. Mionić, A. Magrez, L. Forró, Towards electron spin resonance of mechanically exfoliated graphene, Phys. Status Solidi (B) 246 (11–12) (2009) 2558–2561.
[21] M.A. Augustyniak-Jabłokow, R. Fedaruk, R. Strzelczyk, L. Majchrzycki, Identification of a slow relaxing paramagnetic center in graphene oxide, Appl. Magn. Reson. 50 (2019) 761–768.
[22] A. Diamantopoulou, S. Glenis, G. Zolnierkiwicz, N. Guskos, V. Likodimos, Magnetism in pristine and chemically reduced graphene oxide, J. Appl. Phys. 121 (4) (2017), 043906.
[23] K. Tadyszak, M.A. Augustyniak-Jabłokow, A.B. Więckowski, L. Najder-Kozdrowska, R. Strzelczyk, B. Andrzejewski, Origin of electron paramagnetic resonance signal in anthracite, Carbon 94 (2015) 53–59.
[24] L. Ćirić, A. Sienkiewicz, R. Gaál, J. Jaćimović, C. Vâju, A. Magrez, L. Forró, Defects and localization in chemically-derived graphene, Phys. Rev. B 86 (19) (2012) 195139.
[25] Y. Liu, N. Tang, X. Wan, Q. Feng, M. Li, Q. Xu, F. Liu, Y. Du, Realization of ferromagnetic graphene oxide with high magnetization by doping graphene oxide with nitrogen, Sci. Rep. 3 (2013) 2566.
[26] Y. Liu, Q. Feng, N. Tang, X. Wan, F. Liu, L. Lv, Y. Du, Increased magnetization of reduced graphene oxide by nitrogen-doping, Carbon 60 (2013) 549–551.
[27] Y. Li, Z. Zhou, P. Shen, Z. Chen, Spin gapless semiconductor–metal–half-metal properties in nitrogen-doped zigzag graphene nanoribbons, ACS Nano 3 (7) (2009) 1952–1958.
[28] A.P. Alegaonkar, A. Kumar, S.H. Patil, K.R. Patil, S.K. Pardeshi, P.S. Alegaonkar, Spin transport and magnetic correlation parameters for graphene-like nanocarbon sheets doped with nitrogen, J. Phys. Chem. C 117 (51) (2013) 27105–27113.
[29] M.D. Levi, G. Salitra, N. Levy, D. Aurbach, J. Maier, Application of a quartz-crystal microbalance to measure ionic fluxes in microporous carbons for energy storage, Nat. Mater. 8 (2009) 872.
[30] A.C. Forse, C. Merlet, J.M. Griffin, C.P. Grey, New perspectives on the charging mechanisms of supercapacitors, J. Am. Chem. Soc. 138 (18) (2016) 5731–5744.
[31] J.M. Griffin, A.C. Forse, W.Y. Tsai, P.L. Taberna, P. Simon, C.P. Grey, In situ NMR and electrochemical quartz crystal microbalance techniques reveal the structure of the electrical double layer in supercapacitors, Nat. Mater. 14 (2015) 812.
[32] Alexander C. Forse, John M. Griffin, C. Merlet, J. Carretero-Gonzalez, A.-Rahman O. Raji, Nicole M. Trease, Clare P. Grey, Direct observation of ion dynamics in supercapacitor electrodes using in situ diffusion NMR spectroscopy, Nat. Energy 2 (2017) 16216.
[33] B. Kastening, M. Hahn, B. Rabanus, M. Heins, U. zum Felde, Electronic properties and double layer of activated carbon, Electrochim. Acta 42 (18) (1997) 2789–2799.
[34] J.R. Harbour, M.J. Walzak, P. Julien, Localized paramagnetism in carbon blacks: inherent vs electrochemically reduced sites, Carbon 23 (2) (1985) 185–191.
[35] J.R. Harbour, M.J. Walzak, Electrochemical generation of narrow conduction electron spin resonance signals in carbon blacks, Carbon 24 (6) (1986) 743–745.
[36] J.R. Harbour, M.J. Walzak, Effect of electroreduction on the EPR spectra due to charge carriers in carbon blacks, Carbon 23 (6) (1985) 687–690.
[37] J.R. González, R. Alcántara, J.L. Tirado, A.J. Fielding, R.A.W. Dryfe, Electrochemical interaction of few-layer molybdenum disulfide composites vs sodium: new insights on the reaction mechanism, Chem. Mater. 29 (14) (2017) 5886–5895.
[38] B. Wang, A.J. Fielding, R.A.W. Dryfe, In situ electrochemical electron paramagnetic resonance spectroscopy as a tool to probe electrical double layer capacitance, Chem. Commun. 54 (31) (2018) 3827–3830.
[39] S. Gu, S. Wu, L. Cao, et al., Tunable redox chemical and stability of radical intermediates in 2D covalent organic frameworks for high performance sodium ion batteries, J. Am. Chem. Soc. 141 (2019) 9623–9628.
[40] M. Sathiya, J.B. Leriche, E. Salager, D. Gourier, J.M. Tarascon, H. Vezin, Electron paramagnetic resonance imaging for real-time monitoring of Li-ion batteries, Nat. Commun. 6 (2015) 6276.
[41] B. Wang, A.J. Fielding, R.A.W. Dryfe, Electron paramagnetic resonance investigation of the structure of graphene oxide: pH-dependence of the spectroscopic response, ACS Appl. Nano Mater. 2 (2018) 19–27.
[42] P. Iamprasertkun, A. Krittayavathananon, M. Sawangphruk, N-doped reduced graphene oxide aerogel coated on carboxyl-modified carbon fiber paper for high-performance ionic-liquid supercapacitors, Carbon 102 (2016) 455–461.
[43] Y. Xu, K. Sheng, C. Li, G. Shi, Self-assembled graphene hydrogel via a one-step hydrothermal process, ACS Nano 4 (7) (2010) 4324–4330.
[44] Y. Sun, Q. Wu, G. Shi, Graphene based new energy materials, Energy Environ. Sci. 4 (4) (2011) 1113–1132.
[45] Y. Zou, I.A. Kinloch, R.A.W. Dryfe, Nitrogen-doped and crumpled graphene sheets with improved supercapacitance, J. Mater. Chem. A 2 (45) (2014) 19495–19499.
[46] H.L. Guo, P. Su, X. Kang, S.K. Ning, Synthesis and characterization of nitrogen-doped graphene hydrogels by hydrothermal route with urea as reducing-doping agents, J. Mater. Chem. A 1 (6) (2013) 2248–2255.
[47] H. Seo Min, M. Choi Sung, J. Lim Eun, H. Kwon In, K. Seo Joon, H. Noh Seung, B. Kim Won, B. Han, Toward new fuel cell support materials: a theoretical and experimental study of nitrogen-doped graphene, ChemSusChem 7 (9) (2014) 2609–2620.
[48] J.W. Jang, C.E. Lee, S.C. Lyu, T.J. Lee, C.J. Lee, Structural study of nitrogen-doping effects in bamboo-shaped multiwalled carbon nanotubes, Appl. Phys. Lett. 84 (15) (2004) 2877–2879.
[49] C.S. Lim, C.K. Chua, M. Pumera, Detection of biomarkers with graphene nanoplatelets and nanoribbons, Analyst 139 (5) (2014) 1072–1080.
[50] S.S. Rao, A. Stesmans, Y. Wang, Y. Chen, Direct ESR evidence for magnetic behavior of graphite oxide, Phys. E 44 (6) (2012) 1036–1039.
[51] [a] O.E. Andersson, B.L.V. Prasad, H. Sato, T. Enoki, Y. Hishiyama, Y. Kaburagi, M. Yoshikawa, S. Bandow, Structure and electronic properties of graphite nanoparticles, Phys. Rev. B 58 (24) (1998) 16387–16395;
[b] M.A. Augustyniak-Jabłokow, K. Tadyszak, M. Maćkowiak, S. Lijewski, ESR study of spin relaxation in graphene, Chem. Phys. Lett. 557 (2013) 118–122.
[52] O. Chauvet, G. Baumgartner, M. Carrard, W. Bacsa, D. Ugarte, Walt A. de Heer, L. Forró, ESR study of potassium-doped aligned carbon nanotubes, Phys. Rev. B 53 (21) (1996) 13996–13999.
[53] L. Ćirić, A. Sienkiewicz, D.M. Djokić, R. Smajda, A. Magrez, T. Kaspar, R. Nesper, L. Forró, Size dependence of the magnetic response of graphite oxide and graphene flakes - an electron spin resonance study, Phys. Status Solidi (B) 247 (11-12) (2010) 2958–2961.
[54] A. Ejigu, I.A. Kinloch, E. Prestat, R.A.W. Dryfe, A simple electrochemical route to metallic phase trilayer MoS_2: evaluation as electrocatalysts and supercapacitors, J. Mater. Chem. A 5 (22) (2017) 11316–11330.
[55] M. Seredych, D. Hulicova-Jurcakova, G.Q. Lu, T.J. Bandosz, Surface functional groups of carbons and the effects of their chemical character, density and accessibility to ions on electrochemical performance, Carbon 46 (11) (2008) 1475–1488.
[56] D. Hulicova-Jurcakova, M. Seredych, Q. Lu Gao, J. Bandosz Teresa, Combined effect of nitrogen- and oxygen-containing functional groups of microporous activated carbon on its electrochemical performance in supercapacitors, Adv. Funct. Mater. 19 (3) (2009) 438–447.
[57] X. Wang, X. Li, L. Zhang, Y. Yoon, P.K. Weber, H. Wang, J. Guo, H. Dai, N-Doping of graphene through electrothermal reactions with ammonia, Science 324 (5928) (2009) 768.
[58] B. Náfrádi, M. Choucair, L. Forró, Spin lifetime of itinerant electrons in chemically synthesized graphene multi-layers, Carbon 74 (2014) 346–351.
[59] C.C. Ma, X.H. Shao, D.P. Cao, Nitrogen-doped graphene nanosheets as anode materials for lithium ion batteries, a first-principles study, J. Mater. Chem. 22 (18) (2012) 8911–8915.
[60] Y. Ma, A.S. Foster, A.V. Krasheninnikov, R.M. Nieminen, Nitrogen in graphite and carbon nanotubes: magnetism and mobility, Phys. Rev. B 72 (20) (2005) 205416/1–205416/6.
[61] K. Tanaka, M. Kobashi, H. Sanekata, A. Takata, T. Yamabe, S. Mizogami, K. Kawabata, J. Yamauchi, Peculiar magnetic property of pyrolytic carbon prepared from adamantane, J. Appl. Phys. 71 (2) (1992) 836–841.
[62] P.C. Mundru, V. Pappakrishnan, D.A. Genov, Material- and geometry-independent multishell cloaking device, Phys. Rev. B 85 (4) (2012), 045402.
[63] Y. Deng, Y. Xie, K. Zou, X. Ji, Review on recent advances in nitrogen-doped carbons: preparations and applications in supercapacitors, J. Mater. Chem. A 4 (4) (2016) 1144–1173.
[64] Y.H. Lee, K.H. Chang, C.C. Hu, Differentiate the pseudocapacitance and double-layer capacitance contributions for nitrogen-doped reduced graphene oxide in acidic and alkaline electrolytes, J. Power Sources 227 (2013) 300–308.
[65] F. Beuneu, C. l'Huillier, J.P. Salvetat, J.M. Bonard, L. Forró, Modification of multiwall carbon nanotubes by electron irradiation: an ESR study, Phys. Rev. B 59 (1999) 5945–5949.
[66] N. Fujita, D. Matsumoto, Y. Sakurai, K. Kawahara, H. Ago, T. Takenobu, K. Marumoto, Direct observation of electrically induced Pauli paramagnetism in single-layer graphene using ESR spectroscopy, Sci. Rep. 6 (2016) 34966.
[67] O. Ornelas, J.M. Sieben, R. Ruiz-Rosas, E. Morallón, D. Cazorla-Amorós, J. Geng, N. Soin, E. Siores, B.F.G. Johnson, On the origin of the high capacitance of nitrogen-containing carbon nanotubes in acidic and alkaline electrolytes, Chem. Commun. 50 (77) (2014) 11343–11346.
[68] D. Hulicova-Jurcakova, M. Kodama, S. Shiraishi, H. Hatori, Z.H. Zhu, G.Q. Lu, Nitrogen-enriched nonporous carbon electrodes with extraordinary supercapacitance, Adv. Funct. Mater. 19 (11) (2009) 1800–1809.
[69] Z.H. Zhu, H. Hatori, S.B. Wang, G.Q. Lu, Insights into hydrogen atom adsorption on and the electrochemical properties of nitrogen-substituted carbon materials, Jo. Phys.l Chem. B 109 (35) (2005) 16744–16749.
[70] D. Qu, Studies of the activated carbons used in double-layer supercapacitors, J. Power Sources 109 (2) (2002) 403–411.